Micro-Raman spectroscopic visualization of lattice vibrations and strain in He^{+}- implanted single-crystal LiNbO₃

Hsu-Cheng Huang,[1,*] Jerry I. Dadap,[2] Irving P. Herman,[2] Hassaram Bakhru,[3] and Richard M. Osgood, Jr.[1,2]

[1]Department of Electrical Engineering, Columbia University, New York, New York, 10027, USA
[2]Department of Applied Physics and Applied Mathematics, Columbia University, New York, New York, 10027, USA
[3]College of Nanoscale Science and Engineering, SUNY at Albany, Albany, New York 12203, USA
[*]hh2362@columbia.edu

Abstract: Scanning micro-Raman spectroscopy has been utilized to image and investigate strain in He^{+}-implanted congruent LiNbO₃ samples. By using abruptly patterned implanted samples, we show that the spatial two-dimensional mapping of the Raman spectral peaks can be used to image the strain distribution and determine its absolute magnitude. We demonstrate that both short- and long-range length-scale in-plane and out-of-plane strain and stress states can be determined using the secular equations of phonon-deformation-potential theory. We also show that two-dimensional Raman imaging can be used to visualize the relaxation of strain in the crystal during low-temperature annealing.

©2014 Optical Society of America

OCIS codes: (130.3730) Lithium niobate; (160.4670) Optical materials; (300.6450) Spectroscopy, Raman; (310.3840) Materials and process characterization.

References and links

1. M. E. Lines and A. M. Glass, *Principles and Applications of Ferroelectrics and Related Materials* (Oxford University, 2001).
2. A. Guarino, G. Poberaj, D. Rezzonico, R. Degl'Innocenti, and P. Günter, "Electro-optically tunable microring resonators in lithium niobate," Nat. Photonics **1**(7), 407–410 (2007).
3. M. Roussey, M.-P. Bernal, N. Courjal, and F. I. Baida, "Experimental and theoretical characterization of a lithium niobate photonic crystal," Appl. Phys. Lett. **87**(24), 241101 (2005).
4. F. Chen, X.-L. Wang, and K.-M. Wang, "Development of ion-implanted optical waveguides in optical materials: A review," Opt. Mater. **29**(11), 1523–1542 (2007).
5. M. Levy, R. M. Osgood, Jr., R. Liu, L. E. Cross, G. S. Cargill, A. Kumar, and H. Bakhru, "Fabrication of single-crystal lithium niobate films by crystal ion slicing," Appl. Phys. Lett. **73**(16), 2293 (1998).
6. F. Schrempel, Th. Gischkat, H. Hartung, E. B. Kley, and W. Wesch, "Ion beam enhanced etching of LiNbO₃," Nucl. Instrum. Methods Phys. Res. B **250**(1–2), 164–168 (2006).
7. A. Kling, M. F. da Silva, J. C. Soares, P. F. P. Fichtner, L. Amaral, and F. Zawislak, "Defect evolution and characterization in He-implanted LiNbO₃," Nucl. Instrum. Methods Phys. Res. B **175–177**(0), 394–397 (2001).
8. A. Meldrum, L. A. Boatner, W. J. Weber, and R. C. Ewing, "Amorphization and recrystallization of the ABO₃ oxides," J. Nucl. Mater. **300**(2-3), 242–254 (2002).
9. T. A. Ramadan, M. Levy, and R. M. Osgood, Jr., "Electro-optic modulation in crystal-ion-sliced z-cut LiNbO₃ thin films," Appl. Phys. Lett. **76**(11), 1407 (2000).
10. A. Ródenas, A. H. Nejadmalayeri, D. Jaque, and P. Herman, "Confocal Raman imaging of optical waveguides in LiNbO₃ fabricated by ultrafast high-repetition rate laser-writing," Opt. Express **16**(18), 13979–13989 (2008).
11. J. G. Scott, S. Mailis, C. L. Sones, and R. W. Eason, "A Raman study of single-crystal congruent lithium niobate following electric-field repoling," Appl. Phys. A: Mater. **79**(3), 691–696 (2004).
12. P. Capek, G. Stone, V. Dierolf, C. Althouse, and V. Gopolan, "Raman studies of ferroelectric domain walls in lithium tantalate and niobate," Phys. Status Solidi C **4**(3), 830–833 (2007).
13. G. Stone and V. Dierolf, "Influence of ferroelectric domain walls on the Raman scattering process in lithium tantalate and niobate," Opt. Lett. **37**(6), 1032–1034 (2012).
14. P. S. Zelenovskiy, M. D. Fontana, V. Y. Shur, P. Bourson, and D. K. Kuznetsov, "Raman visualization of micro- and nanoscale domain structures in lithium niobate," Appl. Phys., A Mater. Sci. Process. **99**(4), 741–744 (2010).

15. J. Olivares, A. García-Navarro, G. García, F. Agulló-López, F. Agulló-Rueda, A. García-Cabañes, and M. Carrascosa, "Buried amorphous layers by electronic excitation in ion-beam irradiated lithium niobate: Structure and kinetics," J. Appl. Phys. **101**(3), 033512 (2007).
16. D. Jaque, F. Chen, and Y. Tan, "Scanning confocal fluorescence imaging and micro-Raman investigations of oxygen implanted channel waveguides in Nd:MgO:LiNbO$_3$," Appl. Phys. Lett. **92**(16), 161908 (2008).
17. N. Dong, D. Jaque, F. Chen, and Q. Lu, "Second harmonic and Raman imaging of He$^+$ implanted KTiOPO$_4$ waveguides," Opt. Express **19**(15), 13934–13939 (2011).
18. M. Quintanilla, E. M. Rodríguez, E. Cantelar, F. Cussó, and C. Domingo, "Micro-Raman characterization of Zn-diffused channel waveguides in Tm^{3+}:LiNbO$_3$," Opt. Express **18**(6), 5449–5458 (2010).
19. I. De Wolf, "Micro-Raman spectroscopy to study local mechanical stress in silicon integrated circuits," Semicond. Sci. Technol. **11**(2), 139–154 (1996).
20. T. Tanabe, K. Nishiguchi, A. Shinya, E. Kuramochi, H. Inokawa, M. Notomi, K. Yamada, T. Tsuchizawa, T. Watanabe, H. Fukuda, H. Shinojima, and S. Itabashi, "Fast all-optical switching using ion-implanted silicon photonic crystal nanocavities," Appl. Phys. Lett. **90**(3), 031115 (2007).
21. D. G. Schlom, L.-Q. Chen, C.-B. Eom, K. M. Rabe, S. K. Streiffer, and J.-M. Triscone, "Strain tuning of ferroelectric thin films," Annu. Rev. Mater. Res. **37**(1), 589–626 (2007).
22. J. Ziegler, 2008, *http://www.srim.org*.
23. I. R. Lewis and H. Edwards, *Handbook of Raman Spectroscopy: From the Research Laboratory to the Process Line* (Marcel Dekker, 2001).
24. K. K. Wong, ed., *Properties of Lithium Niobate* (INSPEC, The Institution of Electrical Engineers, 2002).
25. S. M. Kostritskii and P. Moretti, "Micro-Raman study of defect structure and phonon spectrum of He-implanted LiNbO$_3$ waveguides," Phys. Status Solidi C **1**(11), 3126–3129 (2004).
26. H.-C. Huang, J. I. Dadap, O. Gaathon, I. P. Herman, R. M. Osgood, Jr., S. Bakhru, and H. Bakhru, "A micro-Raman spectroscopic investigation of He$^+$-irradiation damage in LiNbO$_3$," Opt. Mater. Express **3**(2), 126–142 (2013).
27. V. Caciuc, A. V. Postnikov, and G. Borstel, "Ab initio structure and zone-center phonons in LiNbO$_3$," Phys. Rev. B **61**(13), 8806–8813 (2000).
28. Y. Repelin, E. Husson, F. Bennani, and C. Proust, "Raman spectroscopy of lithium niobate and lithium tantalate. Force field calculations," J. Phys. Chem. Solids **60**(6), 819–825 (1999).
29. B. Mihailova, I. Savatinova, I. Savova, and L. Konstantinov, "Modeling of Raman spectra of H:LiNbO$_3$," Solid State Commun. **116**(1), 11–15 (2000).
30. E. Zolotoyabko, Y. Avrahami, W. Sauer, T. H. Metzger, and J. Peisl, "Strain profiles in He-implanted waveguide layers of LiNbO$_3$ crystals," Mater. Lett. **27**(1–2), 17–20 (1996).
31. D. Djukic, R. M. Roth, R. M. Osgood, Jr., K. Evans-Lutterodt, H. Bakhru, S. Bakhru, and D. Welch, "X-ray microbeam probing of elastic strains in patterned He$^+$ implanted single-cyrstal LiNbO$_3$," Appl. Phys. Lett. **91**(11), 112908 (2007).
32. M. R. Tejerina, D. Jaque, and G. A. Torchia, "μ-Raman spectroscopy characterization of LiNbO$_3$ femtosecond laser written waveguides," J. Appl. Phys. **112**(12), 123108 (2012).
33. G. Pezzotti, H. Hagihara, and W. Zhu, "Quantitative investigation of Raman selection rules and validation of the secular equation for trigonal LiNbO$_3$," J. Phys. D Appl. Phys. **46**(14), 145103 (2013).
34. R. V. Damie, "Elastic constants of lithium niobate," J. Phys. D Appl. Phys. **25**(7), 1091–1095 (1992).
35. A. Ofan, L. Zhang, O. Gaathon, S. Bakhru, H. Bakhru, Y. Zhu, D. Welch, and R. M. Osgood, Jr., "Spherical solid He nanometer bubbles in an anisotropic complex oxide," Phys. Rev. B **82**(10), 104113 (2010).
36. A. de Bernabé, C. Prieto, and A. de Andrés, "Effect of stoichiometry on the dynamic mechanical properties of LiNbO$_3$," J. Appl. Phys. **79**(1), 143 (1996).
37. D. A. Freedman, D. Roundy, and T. A. Arias, "Elastic effects of vacancies in strontium titanate: Short- and long-range strain fields, elastic dipole tensors, and chemical strain," Phys. Rev. B **80**(6), 064108 (2009).
38. M. A. Carpenter, R. E. A. McKnight, C. J. Howard, Q. Zhou, B. J. Kennedy, and K. S. Knight, "Characteristic length scale for strain fields around impurity cations in perovskites," Phys. Rev. B **80**(21), 214101 (2009).

1. Introduction

Complex oxides, particularly those having perovskite and perovskite-like structure with chemical formula ABO$_3$ ('A' and 'B' are two different metal cations) exhibit important material functionality such as ferroelectricity, piezoelectricity, and electro-optic and high dielectric response [1]. Lithium niobate (LiNbO$_3$) is one of the most widely used materials among this group, with many applications in photonic-related microdevices such as electro-optically tunable micro-ring resonators [2] and photonic crystals [3]. In several recent cases, these applications have involved the use of ion implantation for materials processing, including refractive-index tuning for waveguiding [4] and crystal ion slicing for fabrication of ultrathin films of these materials [5]. However, it is well known that ion-processing-induced changes can, at the same time, lead to degradation of the desired material properties. These changes include the formation of defect clusters, bond scission, surface blistering, and

volumetric swelling [6,7]. Thus the study of this damage and the procedures for alleviating it are important for high-performance devices as well as for a general understanding of the materials science of these crystals. For example, the temperature dependence of amorphization and recrystallization behavior has also been studied in other ABO_3 oxides such as $LiTaO_3$, $SrTiO_3$, and $BaTiO_3$ [8]. In addition, radiation damage itself, including that stemming from ion bombardment, is also an important issue for understanding the robustness of these materials to a radiation environment. As an example, radiation damage and any concomitant stress can play a role in changing the polarization properties [9] of travelling electromagnetic waves in implanted electro- or acousto-optical devices.

Micro-Raman imaging is a powerful nondestructive approach to examine lattice modification and local micro-structural change. Pioneering work in this area includes the observation of local lattice dilatation following ultrafast high-repetition-laser writing in $LiNbO_3$ crystals [10], the visualization of micro- and nanoscale domain structures from high-electric-field and pulse-laser-irradiation poling also of $LiNbO_3$ and $LiTaO_3$ [11−14], and the observation of buried amorphous layers or lattice rearrangements in doped or undoped $LiNbO_3$ and other crystalline oxides such as $KTiOPO_4$ (KTP) formed via ion irradiation or ion in-diffusion [15−18]. Despite these insights, however, important open questions still remain of the capabilities and interpretation of micro-Raman imaging. One pressing question is its utility in probing an implantation-induced strain field and stress states at abrupt irradiation interfaces, and how this potentially sharp distribution is changed in the presence of post-irradiation treatment. This information is crucial, for example, when patterning implantation is required, such as in silicon integrated optical or electronic circuits [19] or in the fabrication of photonic-crystal nanocavities [20]. Such information also elucidates strain-enabled material properties including strain-tuning ferroelectricity [21] and the potential applications of strained optoelectronic devices. Note that several recent reports including one from our laboratory have shown that strain fields can be imaged using micro-Raman methods but a quantitative study using well-defined continuum modeling has thus far not been realized.

In this paper, we demonstrate that probing of abrupt implantation boundaries of interfaces can provide a model structure to investigate strain fields. Two-dimensional (2D) scanning micro-Raman spectroscopy was used to show that crystal strain field resulting from ~MeV He^+ patterned implant of $LiNbO_3$ can be fully imaged and quantitatively analyzed from surface to deeper unimplanted region, and compared to an accurate simulation based on the use of secular equations of phonon-deformation-potential theory. We show that ***both*** short- and long-range in-plane and out-of-plane strain distribution can be measured explicitly and compared to a simulation based on a continuum-model computation. We also show the stress field, including that at the irradiation boundary, can be calculated with different step resolutions from ~200 − 1000 nm. The relations of crystalline damage (lattice disorder) and induced strain, experimentally shown by an implantation-induced Raman linewidth and Raman shift, are also discussed. This micro-Raman approach thus allows strain and stress fields near or at mask-patterned interfaces following high-energy implantation to be visualized with high-resolution.

2. Experimental

In the experiments, congruent single-crystal Z-cut $LiNbO_3$ samples (Crystal Technology) were used. Prior to implantation, the samples were bonded to a water-cooled holder with silver paste in order to remain at ambient temperature during processing and then they are implanted with He^+ ions through the Z + surface at a 7° tilt angle from normal to prevent ion channeling. The incident ion energy was 3.8 MeV and the samples were implanted with a total dose of 5×10^{16} cm^{-2}. *SRIM* (Stopping and Range of Ions in Matter) simulations [22] show that this ion energy yields a stopping range of ~10 μm below the surface with a ~450-nm straggle. In cases of patterned implantation, a 0.5-mm-thick metal proximity mask with

circular-grid openings (with diameters of ~500 μm) was placed on the surface of the sample so that only the circular regions were exposed to He$^+$. After implantation, selected samples were annealed at temperatures ranging from 150° to 600°C under laboratory-ambient conditions to study the crystallinity-recovery dynamics. The sample edge facets were polished carefully until an optical finish (~λ/5) was achieved for realization of an unambiguous backscattered Raman signal.

Our Raman spectroscopy apparatus (*Renishaw inVia*) used a diode-laser-based-excitation wavelength of 532 nm, with the laser beam focused by a 100 × microscope objective (NA = 0.85) in a confocal geometry so as to achieve a spot size ≤ 1 μm. The spectral resolution was ~1.5 cm^{-1}, using an 1800 lines/mm grating. Raman probing was done by first scanning along the polished facet, i.e., along the crystal Z-axis, with the incident polarization in the Z-axis, or, in Porto notation [23], *X(Z,ZY)* $\overline{X}$, to acquire changes in the Raman damage profile as a function of implantation depth. The inset in Fig. 1(a) shows a sketch of this edge-probing geometry, with the capital letters in the sketch indicating the probing locations. In this orientation, the A$_1$(TO) (254, 276, 332, and 631 cm^{-1}) and the E(TO) (152, 236, 263, 322, 365, 432, and 581 cm^{-1}) phonon modes are active, according to standard Raman selection rules [24]. Note that prior to ion bombardment, a scan on unirradiated LiNbO$_3$ was first employed to investigate the sample homogeneity. The spectra obtained from the virgin sample agree with the active Raman phonon modes as reported in literature. The results of irradiated samples are thus compared with the virgin case and discussed below. In order to rule out contributions from high k-parallel contributions of the Raman signals, which may occur for the large-N.A. microscope objective used, we compared spectra obtained with lower-N.A. objective lenses (N.A. = 0.25, 0.40 and 0.75). The results for all N.A. values show the same peaks that are unshifted and no new peaks appeared for the highest N.A.

3. Results and discussion

To briefly review, as reported earlier in [25] and as seen also in the present measurements, if a crystal is subjected to ion bombardment, hence causing the formation of point and extended defects, there is a sharp change in the Raman spectra. Thus in the present measurements, as the probe scans along the Z direction into the stopping range, the modal intensity of an allowed Raman feature decreases and its linewidth broadens. Concomitantly normally forbidden-mode signals appear and grow in intensity [26]. In addition, the position of the peak of spectral feature shifts, particularly for the active modes A$_1$(TO$_1$) at 254 cm^{-1} and A$_1$(TO$_4$) at 631 cm^{-1}; these shifts are indicated in Fig. 1(a) by the dashed lines. The A$_1$(TO) modes originate from displacements and vibrations of Li and Nb ions along the Z-axis as well as distortions of the oxygen octahedron in the XY plane [27–29]. With these vibrational assignments, the implantation-induced modifications in each of the A$_1$(TO) modes in Fig. 1(a) indicate that He$^+$ implantation causes damage in each of the three Cartesian directions.

Lorentzian peak fittings were carried out to obtain peak positions and linewidths. Figures 1(b) and 1(c) show data taken for the A$_1$(TO$_4$) mode, along with the Lorentzian fits for data from variation of depth in the crystal and annealing temperature. In particular, Fig. 1(b) shows the spectra of the A$_1$(TO$_4$) mode at different positions along Z-axis. A plot of the peak spectral position and linewidth (FWHM) along the Z-axis is shown in the inset; Fig. 1(c) shows the effects of annealing for ~10 hours on the A$_1$(TO$_4$) mode spectrum at the stopping range, i.e., point H, with the spectral position and linewidth versus temperature plotted in the inset. Notice that in the inset of Fig. 1(b), the plots show that the spectral shifts and broadening extend many tens of micrometers beyond the region of high implantation inclusions and damage (red and black dotted lines). However, the *SRIM* calculated defect distribution (blue dotted curve) is only ~1 μm in width. This apparent extension of the damage toward surface is attributed to the implantation-induced strain. It is clear that the strain results in a peak redshift, with the greatest magnitude at the stopping range (~10 μm

from the surface, labeled H), where the density of defects is maximum. The presence of a shifted spectrum indicates that there is a change in the local lattice constants [23]. In experiments using patterned implantation, i.e., an implantation region surrounded by virgin crystal, earlier X-ray diffraction measurements [30,31] and analytic theory have suggested that the implanted region is under compressive stress in the X-Y plane, due to the He-atom inclusions. This stress leads to tension in the Z direction via the stress field, resulting in a change in surface topography. In our case, the redshift of the $A_1(TO_4)$ mode is ~8 cm^{-1} (see Fig. 1(b)). A separate experiment using Z-scan geometry $Z(X, XY)\overline{Z}$ (not shown here, see [26]) revealed that at the helium stopping range, the $A_1(LO_4)$ mode at ~875 cm^{-1} has a blueshift of ~2 cm^{-1}. Given these two spectral shifts, we can extract local strain information by using deformation potential theory.
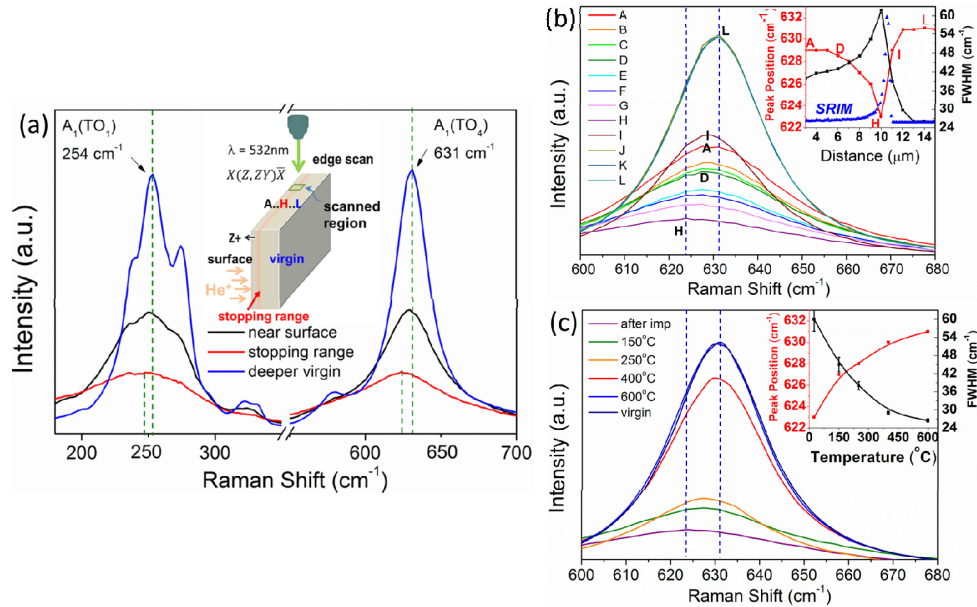

Fig. 1. (a) Examples of Raman spectra obtained at different probing locations: near-surface (black, labeled A in inset sketch), stopping range (red, labeled H), and deeper in the unimplanted crystal (blue, labeled L). A decrease of phonon modal signal is clearly seen in the irradiated regions. Peak shifts for $A_1(TO_1)$ at 254 cm^{-1} and $A_1(TO_4)$ at 631 cm^{-1} modes are indicated by dashed lines. Inset: sketch of micro-Raman edge-probing geometry. Capital letters on the sample sketch indicate specific scan positions. He$^+$ stopping range is ~10 μm below the surface. (b) Peak shift as a function of probing distance; the maximum is observed at the He$^+$ stopping range. Inset: peak position and linewidth as a function of the probing distance; blue dotted curve is *SRIM*-simulated defect distribution. Peak fits using a Lorentzian function, exhibit a total redshift of ~8 cm^{-1} (c) Upon annealing, crystal defects are "healed" and the elastic strain relieved (see inset) for 600°C annealing for ~10 hours.

Because the nondiagonal A_1 Raman tensor elements of LiNbO$_3$ are zero for an ideal crystal, linear deformation potential theory (secular equation) is applicable. In this theory, the relationship of Raman spectral shifts ($\Delta\omega_{A_{1i}}$) to mechanical deformation from strain (ε) can be expressed as $\Delta\omega_{A_{1i}} = a_{A_{1i}}(\varepsilon_{xx} + \varepsilon_{yy}) + b_{A_{1i}}\varepsilon_{zz}$ [32,33], where $a_{A_{1i}}$ and $b_{A_{1i}}$ are the A_1 phonon deformation potential (PDP) constants. The subscript of A_{1i} indicates different A_1 modes. Using the PDP values in [33] and the spectral shifts obtained in our experiments, we estimate the compressive normal strain on the basal plane ($\varepsilon_{xx} + \varepsilon_{yy}$) and the vertical tensile strain (ε_{zz}) to be ~ $-(2\text{-}5) \times 10^{-3}$ and $(3\text{-}6) \times 10^{-2}$, respectively, where the range in their

values is due to that in the PDP constants. This local inhomogeneous lattice deformation has also been observed in Y-cut LiNbO$_3$ by X-ray diffraction [30]. Applying the LiNbO$_3$ stiffness tensor [34], we can approximate the stress parameters as

$$S_{zz} = C_{13}(\varepsilon_{xx} + \varepsilon_{yy}) + C_{33}\varepsilon_{zz} = 7\text{-}13\,\text{GPa} \tag{1}$$

$$S_{xx} + S_{yy} = (C_{11} + C_{12})(\varepsilon_{xx} + \varepsilon_{yy}) + 2C_{13}\varepsilon_{zz} = 3\text{-}8\,\text{GPa} \tag{2}$$

The ranges of the values of the stress tensor elements are due to the variations in both strain parameters and elastic constants [24]. The order of magnitude of ~10^{10} Pa value for this anisotropic stress state is nearly identical to the value calculated using the elastically isotropic condition [35]. Note that the vibrational mechanisms of A$_1$(TO$_4$) and A$_1$(LO$_4$) modes involve lattice vibrations in all directions (oxygen-octahedron vibration along the XY plane, and Nb-O-bond and Li-O-bond vibrations parallel to Z axis, respectively [10.36]).

In addition, our studies show that the strain can be varied by subsequent thermal processing. This behavior is seen in the fact that the peak position and its width (FWHM) nearly recover to their values in the unimplanted crystal after ~10 hours of 600°C annealing. The peak position and the width can be plotted versus the inverse temperature to extract the characteristic activation energies for the recovery process. The results show an Arrhenius-like behavior with E_a = 0.24 ± 0.02 eV for the recovery of the value of the width of the spectral feature in the unimplanted crystal and E_a = 0.20 ± 0.03 eV for the recovery of the location of its peak position of the spectral feature. The latter quantity can be directly correlated to the energy needed to relieve the strain in the crystal. The interpretation of the measured activation energy for the linewidth is not as clear. However the magnitude of any locally inhomogeneous strain, which could lead to broadening of the linewidth, would clearly be scaled by the overall magnitude of the strain. Thus the agreement of the overall activation energies for strain and linewidth recovery is not unexpected. Note that since broadening can also result from lattice disorder or damaged crystallinity, a more detailed set of experiments must be undertaken before more definitive statements can be made. Two-dimensional (2D) mapping on samples with shadow-mask-patterned implantation was carried out to investigate the spatial distribution of strain. Figure 2(a) shows imaging of the Y-Z plane obtained with 1-µm steps of the Raman probe beam; Roman numerals (I) and (II) indicate regions that are implanted and unimplanted, respectively. Higher-resolution mapping with 250-nm steps was also performed (an example is indicated by the white box in Fig. 2(a)) to enable a detailed investigation of the boundary region. This result is displayed in Fig. 2(b). Note that Figs. 2(a) and 2(b) have the same intensity-color-scale bar. From the variation along the Z axis, it is clear that the peak redshift is maximum at the stopping range (R_p ~10 µm); the location of this plane is indicated by a yellow arrow in Fig. 2(b); in the deeper unimplanted region, the peak position is identical to that in the unimplanted sample. As discussed above, the shifts are attributed to the existence of implantation-induced strain.

More subtle features can also be seen in the micro-Raman strain map. A clear wing-like feature is seen at the border of the implanted patterned region and near the stopping region. This feature is consistent with a comparable feature that has been observed in X-raymicrobeam measurements in ion-implanted channel patterns [30]. The outline of the wing adjacent to the implantation boundary was fitted with a simple polynomial curve (see Fig. 2(b)), which followed the location of the maximum derivative of the signal intensity along the horizontal direction at each Z point above the stopping range. Notice that the stress in this region spreads far into the masked area. Clearly the extent of this stress reflects the stress in the adjacent implanted region, which was shown in Fig. 1(b) above, and thus the wing extends the furthest laterally at the depth of stopping range, where the defect density is the highest. In addition, the optical image, as seen in Fig. 2(c), shows that the implantation is confined to the unmasked region. A relevant theoretical study on the ensemble of vacancy-

defect strain tensors (strain per unit defect concentration induced in a crystal) has also been reported for strontium titanate ($SrTiO_3$) [37].
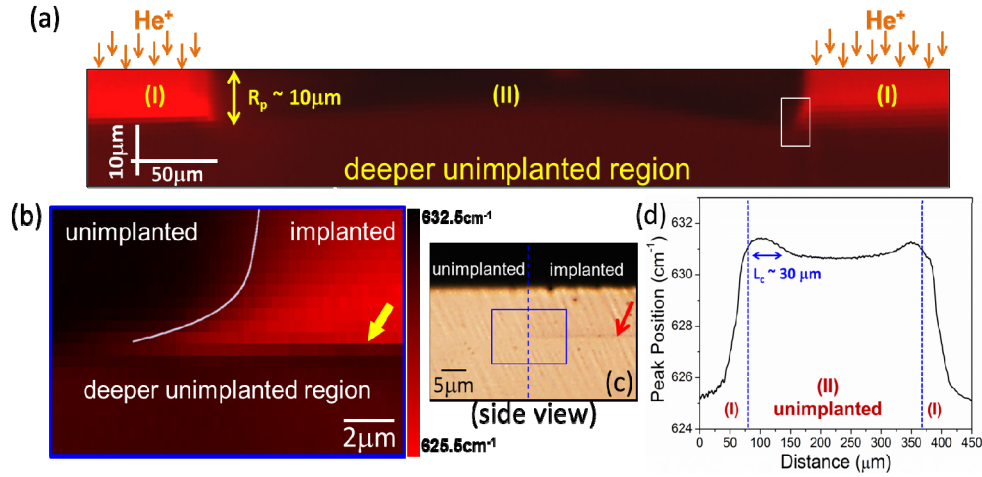

Fig. 2. Two-dimensional (2D) Raman mapping on a patterned-implanted sample: (a) High-contrast imaging of peak positions of the $A_1(TO_4)$ mode between implanted (I) and unimplanted (II) regions. (b) 250-nm-step imaging at implantation interface (white outline in (a)). Yellow arrow indicates plane of largest redshift (coincident with the ion stopping range). Extended "wing" at the implantation edge (marked with white fitted curve). (c) Corresponding optical cross section of this same region, blue outline indicates imaged region in (b); red arrow indicates location of stopping range. (d) 1-μm-step line scan, taken at the depth corresponding to the ion stopping range, across two implanted regions showing the extent of the long-range strain field; blue dashed lines indicate locations of interfaces. A change in peak positions occurs across the implanted region. An apparent $L \sim 30$ μm length scale for strain relaxation is seen for the ~631 cm^{-1} $A_1(TO_4)$ mode.

Figure 2(d) is a separate 1-μm-step line scan, taken at the depth corresponding to the ion stopping range, across two implanted regions to show the extent of the long-range strain field distribution. As can be seen in Fig. 2(d), the signal decreases by over a length scale, $L \sim 30$ μm, as the probe scans across the implantation boundary toward the unimplanted region, where L is defined as the distance between the implantation interface to the position where the peak shift is decreased to $1/e$ of the total shift. The origin and the value of the scale length L at different depths for this strain relaxation is undoubtedly set in part by the total implantation dose and the ion straggle, but has not yet been studied in detail. The existence of such a length scale has also been seen in other perovskites, for other strain-enabled phenomena [38]. Using the secular equation above, we find that for a position ~10 μm away from the implanted boundary, ε_{zz} and $(\varepsilon_{xx} + \varepsilon_{yy})$ are smaller by factors of ~100 and 10, respectively, relative to their maximum values. In addition to imaging the strain distribution, 2D mapping was used to follow the evolution of the damage distribution upon thermal annealing. Figures 3(a)-3(c) are Raman imaging maps of the 631 cm^{-1} active mode in samples, which are as-implanted [Fig. 3(a)], implanted and then annealed at 250°C for 30 minutes [Fig. 3(b)], and implanted and then annealed at 600°C for 30 minutes [Fig. 3(c)]; Figs. 3(d)-3(f) show samples having these same processing conditions for the 875 cm^{-1} forbidden mode. Based on *SRIM* calculations, a dose of 5×10^{16} cm^{-2} will lead to a total vacancy concentration of ~10^{22} cm^{-3}, or ~0.3 *dpa* (displacement per atom). This high *dpa* yields lattice disorder, leading to the appearance of normally forbidden modes while at the same time causing a decrease of the signals from active modes. These counteracting effects lead to the high-contrast imaging in the active/forbidden-mode mapping. Similar phenomena have also been observed in patterned-implanted samples between the implanted and

unimplanted regions [26]. The narrow regions indicated by the yellow arrows in Fig. 3, correspond to the ion range, for which the damage is maximum. After annealing at 250°C, crystallinity is partially recovered [Figs. 3(b) and 3(e)]; further annealing at 600°C facilitates the recovery process such that the width of the narrow regions from nuclear-collision damage is decreased [Figs. 3(c) and 3(f)]. Notice that selected samples were annealed at different temperatures respectively for 30 minutes. Increasing the annealing time further fosters the restoration of crystallinity.
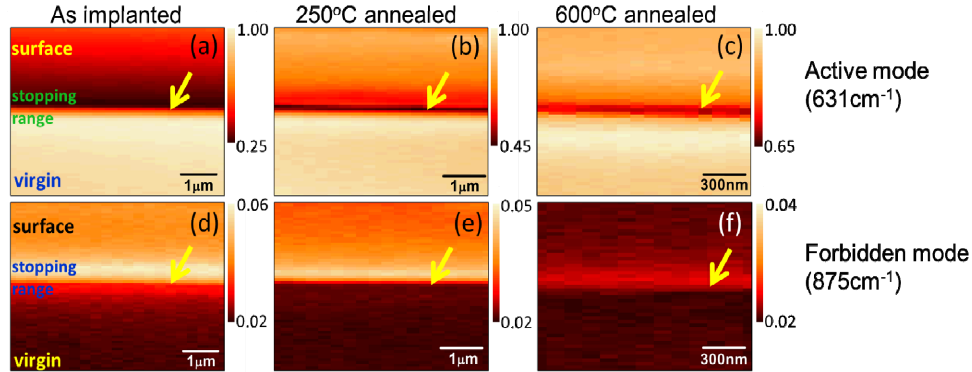

Fig. 3. 2D Raman mapping of the evolution of damage after annealing for 30 minutes at different temperatures. Panels (a,d), (b,e), and (c,f) are Raman images of as-implanted, 250°C-annealed, and 600°C-annealed samples, respectively, using the 631 cm^{-1} active mode (top panels) and 875 cm^{-1} forbidden mode (bottom panels) Raman signals, with arrows indicating the stopping range. For the active (forbidden) mode, the brightest signal indicates high (low) degree of crystallinity.

4. Conclusions

In conclusion, we have shown using Raman spectroscopy the visualization of the formation of a significant crystalline-damage-induced elastic-strain field formed by ~MeV He[+] implantation. This strain field is seen clearly in patterned implanted samples using either a change in the intensity, peak shift, and linewidth of allowed or forbidden Raman modes. High-spatial-resolution 2D mapping of the damaged region permits visualization of the strain and defect distribution, and the crystalline recovery upon annealing. The sharp Raman mapping patterns seen in our samples make it clear that micro-Raman imaging is a powerful tool for observation of strain and stress effects in ion-irradiated oxide samples.

Acknowledgments